Vis Comput (2015) 31:1431–1446
DOI 10.1007/s00371-014-1024-4

ORIGINAL ARTICLE

A parallelized 4D reconstruction algorithm for vascular structures and motions based on energy optimization

Xinglong Liu · Fei Hou · Aimin Hao · Hong Qin

Published online: 19 September 2014

Abstract In this paper, we present a parallel 4D vessel reconstruction algorithm that simultaneously recovers 3D structure, shape, and motion based on multiple views of X-ray angiograms. The fundamental goal is to assist the analysis and diagnosis of interventional surgery in the most efficient way towards interactive and accurate performance. We start with a fully parallelized algorithm to extract vessels as well as their skeletons and topologies from dynamic image sequences. Then, instead of resorting to registration, we present an algorithm to formulate the reconstruction problem as an energy minimization problem with color, coherence, and topology constraints to reconstruct the 3D vessel initially, which is robust to combat noise and incomplete information in images. Next, we incorporate temporal information into our energy optimization framework to track and reconstruct 4D kinematics of the dynamic vessels, which is also capable of recovering previous incomplete and misleading shapes acquired from static images otherwise. We demonstrate our system in coronary arteries reconstruction and movement tracking for percutaneous coronary intervention surgery to help medical practitioners learn about the 3D shapes and their motions of the coronary arteries of specific patient. We envision that our system would be of high assistance for diagnosis and therapy to treat vessel-related diseases in a clinical setting in the near future.

Keywords X-ray angiograms · 3D reconstruction · Motion tracking · Belief propagation

1 Introduction and motivation

The morbidity of cardiovascular disease (CVD) is rapidly increasing over the past few decades. The golden standard for diagnosis of CVD is X-ray coronary angiography which is only offering 2D projection of relevant tissues/organs from 3D space. Yet, X-ray images not only lack a significant amount of 3D information of the coronary arteries, but also suffer from the viewing angle dependence, overlapping and blurring, etc. Accurate and rapid 3D reconstruction from limited views is necessary for medical practitioners towards earlier diagnosis and better treatment. This paper's originality hinges upon our novel and parallel solution to the simultaneous 4D structure, shape, and motion reconstruction from time-labeled image sequences.

Even though various work has been done to tackle the reconstruction problem in X-ray views, there are still some unsolved challenges existing in current methods. First, the noisy and blurry X-ray images may give rise to incorrect reconstruction. Second, accurate reconstructions need five or even more views of angiograms with exact angle requirements, which is hard to operate for clinical use. Third, current 3D reconstruction methods mostly rely on the registration between image pairs, which are less robust and much harder to incorporate with constraints such as consistency, continuity, and coherence. Finally, since there are so many processing procedures involved during analysis and reconstruction, the overall computation is extremely time-consuming.

Electronic supplementary material The online version of this article (doi:10.1007/s00371-014-1024-4) contains supplementary material, which is available to authorized users.

X. Liu · F. Hou (✉) · A. Hao
State Key Laboratory of Virtual Reality Technology and Systems, Beihang University, Beijing, China
e-mail: houfei@vrlab.buaa.edu.cn

H. Qin
Department of Computer Science, Stony Brook University, Stony Brook, USA

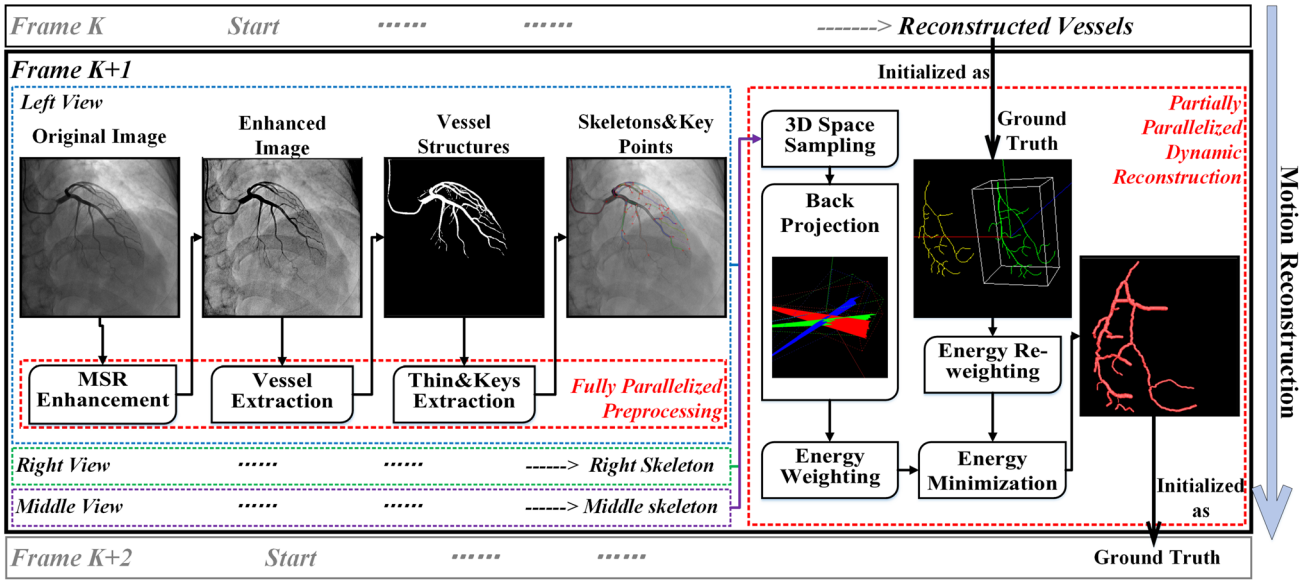

Fig. 1 Work pipeline. *Left part*: image preprocessing. *Right part*: dynamic reconstruction. From frame K to frame $K+1$: reconstruction with time T

To overcome such shortcomings, we present an efficient vessel reconstruction and motion tracking system from multiple X-ray views. The pipeline is shown in Fig. 1 consisting of two stages: vessel extraction (Sect. 3) and 4D reconstruction (Sect. 4). In the first stage, we design a parallel algorithm to extract the vessels as well as their skeletons and topologies. In the second stage, we devise a novel algorithm to reconstruct 4D dynamic vessels robustly to resist noise and combat incomplete information in images. Moreover, the parallel CUDA implementation greatly enhances efficiency in our system. The main contributions of our work include

- An efficient parallelized thinning and refining method for extracting vessel skeletons and key points.
- A novel energy optimization algorithm to reconstruct vessels based on energy optimization solved using belief propagation with color, coherence, and topology constraints, which is robust to noisy and incomplete information from images.
- An improved energy formulation that unites temporal information with spatial information for better recovering 4D kinematics of vessels, whose advantages also include robustness to noisy and incomplete information in static images and ability of repairing misleading shapes.
- A vessel reconstruction and tracking system with the fully parallelized image processing algorithm and partially parallelized Belief Propagation (BP) algorithm.

This paper is organized as follows: Sect. 2 briefly summarizes related work we encounter during reconstruction and tracking. Section 3 details our preprocessing step. Section 4 documents the proposed reconstruction and motion tracking methods. Section 5 discusses the implementation of these parallelized methods. Results, validations, performance, discussion, and conclusions are presented in Sects. 6 and 7.

2 Related work

Our work relates to vessel extraction, vessel reconstruction, etc. We now briefly review them in the following categories.

Vessel extraction. Vessel extraction can be divided into six categories of techniques: pattern recognition techniques (PR), deformable model-based techniques [1,2], tracking-based techniques [3–5], artificial intelligence-based techniques, neural network-based techniques, and miscellaneous tube-like object detection techniques. Each one contains many sub-types such as multi-scale approaches, mathematical morphology approaches. Readers could refer to [6] for an overview. Besides, Hoover et al. [7] used a mathematical filter to offer a broad range of vessel enhancement, and Li et al. [8] conducted this task using a non-linear filter. Frangi et al. [9] used the eigen values of Hessian matrix to extract the tube-like structures from X-ray images. Condurache et al. [10] used this method while adding a hysteresis thresholding method to purify the extracted data. But they are not robust to handle blurry images. Zhang et al. [11] proposed a novel extension of the matched filter approach which is composed of a zero-mean Gaussian function and the first-order derivative of Gaussian, yet their extraction may lead to more isolated retinal vessels.

Skeleton extraction. Normally, centreline extraction for vessels is essential for both data simplification and further

processing. Van et al. [12] and Hassouna et al. [13] proposed methods based on Eikonal Equation and fast marching method to find vessel skeletons. Yet, they could not process isolated vessel segments. Zhang et al. [14] proposed a two-step thinning method based on the structure analysis of the candidate vessel structures. Tracking-based techniques are also popular in this area. Most thinning methods are hard to be parallelized.

3D reconstruction. Definitely, 3D reconstruction from 2D projection images is feasible and reasonable. Wellnhofer et al. [15] and Messanger et al. [16] evaluated that 3D reconstructions of coronary arteries from 2D X-ray image sequences permit accurate results of the real data. Currently, there are two types of X-ray machines, leading to two slightly different ways of 3D reconstruction. The biplane system takes two (mostly) synchronized projection of the coronary arteries [15,16], while the mono-plane (single-plane) system [17] can just take one view at the same time; therefore, selection of asynchronous images from multiple views is needed. Movassaghi et al. [18] used multiple projections for realistic vessel lumen simulation. Sprague et al. [19] utilized the benefits of three projections experimentally. Hansis et al. [20] had used multiple projections from a single rotational X-ray angiography to reconstruct the 3D centerline and the topology. Nguyen et al. [21] proposed a method based on motion and multiple views using a single-plane imaging system. Most of the methods above rely on explicit registration which is rather unstable in the blurry X-ray views and the constraints used by registration are too simplified to take various affecting terms into account. Other routines such as knowledged-based or rule-based methods have been proposed for 3D reconstruction using the vascular network model [22,23]. Since their rules or knowledge is designed for specific conditions, it is not easy to generalize these kinds of methods to process artery data. In [24–26], optimal estimation is investigated with a two-step approach based on maximum-likelihood and minimum-variance estimation. They used a linear algorithm to compute the preliminary estimates as the initial estimates for the process of optimal estimation.

Motion tracking. Prior to the work of Ruan et al. [27], most analysis work focuses on static reconstruction using feature matching techniques. Similar method based on the same prediction-projection-optimization loop is proposed in [28]. In [29], a motion trajectory is computed for each point from the segmented artery tree independently, they used a set of vectors describing the general motion of each artery branch. Chen et al. [30] reconstructed the vessel tree and performed motion tracking on this tree with constraints. Based on the work of Naegel et al. [31], Shechter et al. [32] presented a 3D method for tracking the coronary arteries through a temporal sequence of biplane X-ray angiograms. On the other side, motion field recovered from each data set is composed of patients' heart and breath movements, which could be regarded as a function of cardiac phase and respiratory phase. Shechter et al. [33] proposed a parametric model to decompose the motion field into independent cardiac and respiratory components. Meanwhile, Blondel et al. [34] presented a method to compute 4D tomographic representations of coronary arteries from a single view of rotational monoplane angiograms based on 4D B-spline solids to model motions. Bouattour et al. [35] formulated the tracking problem as a 3D-2D registration problem in which the 3D model deforms in space to best fit the given set of 2D angiogram. In [36], a projection-based motion compensation and reconstruction method of coronary segments and cardiac implantable devices from rotational X-ray angiograms was developed. Most of current tracking methods are either based on 3D to 2D projection or simple 2D registration using simple weighting term, leading to unsatisfactory results and less robustness. Methods based on mathematical analysis can simulate true motion of humans' heart, but they are specific and can not be generalized.

Optimization methods. Energy optimization techniques are widely used in various areas such as image restoration, 3D reconstruction, etc. Geman et al. [37] first proposed the classical theories of Markov Random Field (MRF), Gibbs Sampling and Maximum a Posteriori estimate. Lafferty et al. [38] proposed the Conditional Random Field (CRF) which provides a tool for structural classification and prediction. Based on these theories, BP was proposed by Pearl [39] to solve the optimization problems in MRF. From then on, many applications have been done with the help of BP, including performance studies [40–43], speedup methods [44–47], etc. Besides BP, Graph Cut (GC) is also an energy minimization method which is better in first-order MRF than BP and much better than dynamic programming, gradient decedent, simulated annealing, etc. GC is widely used in computer vision including image segmentation [48], stereo disparity, and motion [49]. In [49], Boykov presented an efficient α-expansion and α-β swap algorithm for metric energy minimization based on GC. Kolmogorov et al. [50] introduced the characteristics of the energy function which could be minimized by GC and conducted the genetic construction of the minimization function. Based on GC, there are many extensions, such as Grow Cut [51], Grab Cut [52] et al. We formulate the vessel reconstruction problem as a discrete energy solved by BP.

3 Vessel and skeleton extraction

Given X-ray angiograms, we design an efficient algorithm to extract the vessels and their skeletons as well as topologies robustly which are readily available for further reconstruction. We present a novel parallel method to extract vessels as

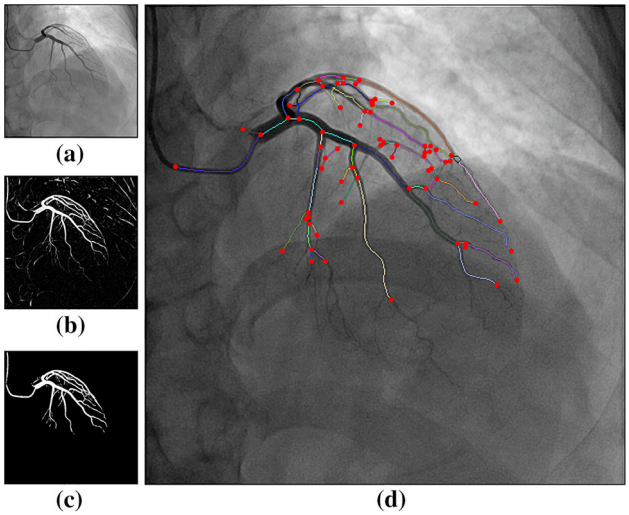

Fig. 2 Vessel extraction results. **a** Original image; **b** possibility image; **c** binary image; **d** enlarged image with *highlighted points* and skeletons

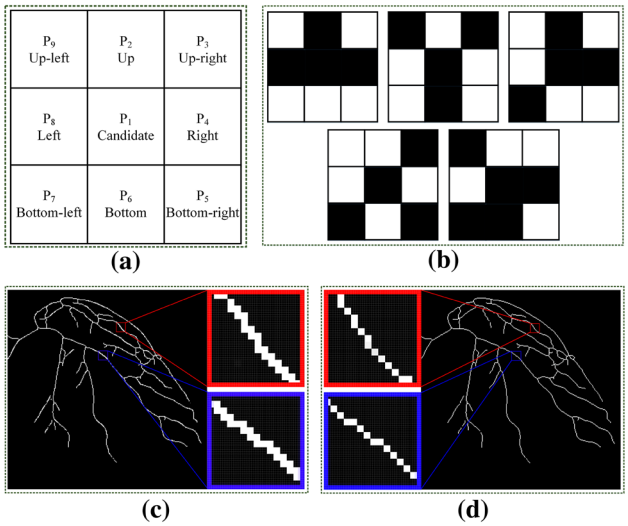

Fig. 3 Thinning refinement. **a** Designations of nine pixels in 3×3 window; **b** bifurcation patterns; **c** rough skeletons; **d** refined skeletons

well as their skeletons (Sect. 3.1) and finally the skeletons are segmented into segments split by bifurcated points to derive the topology structures (Sect. 3.2). All of these steps are run on GPU with great efficiency.

3.1 Vessel and skeleton extraction

Original angiograms acquired from the X-ray machine suffer from low contrast, low lumen, etc. To overcome these problems, we first apply the enhancement of radiography based on multiscale retinex (MSR). Then, we use the gain/offset method to fix the negative values. Finally we convolve the original images by four Gaussian filters with different scales and compute the weighted average of them, giving rise to satisfactory results.

After the enhancement, we extract the vessel skeletons for further vessel reconstruction. We parallelize the algorithm proposed in [9] which relies on a multiscale Hessian matrix and apply it to MSR enhanced angiograms and extract tube-like structures. Extracted vessels can be found in Fig. 2b–c.

To simplify the reconstruction, we use skeletons to present vessel structures. Our skeleton extraction method mainly consists of three steps. First, a typical two-step thinning method is used to extract the rough skeletons. Second, we refine the skeletons to ensure its one-pixel width and use a pattern-based method to extract its bifurcations and end points. At last, we collect the skeletons from bifurcations and derive the entire structure of the skeleton tree. All these three steps are done on GPU with the help of CUDA and achieve great efficiency.

In order to extract the skeleton, we use a two-step local-feature based thinning method [14] to start with. Although the two-step thinning method provides a good initialization, the results are far from ideal enough for extracting the key points and structure of the skeletons because of the redundant points shown in Fig. 3c. We design a novel parallelized method to conduct the refinement while keeping efficiency.

First of all, we label points as *deleted* based on its neighbors. As shown in Fig. 3a, consider P_1 as the candidate, if $P_1 = 1$, P_1 is valid and vice versa. There are four ways that this point should be labeled as *deleted*: (1) $P_2 = P_8 = 1$ and $P_4 = P_5 = P_6 = 0$; (2) $P_2 = P_4 = 1$ and $P_6 = P_7 = P_8 = 0$; (3) $P_4 = P_6 = 1$ and $P_8 = P_9 = P_2 = 0$; (4) $P_6 = P_8 = 1$ and $P_2 = P_3 = P_4 = 0$.

Second, *deleted* information together with point neighbors are used to decide which points should really be deleted. Similarly, consider P_1 as one of the *deleted* labeled points according to Fig. 3a; there are two ways making this point actually be deleted: (1) none of P_2, P_4, P_6, P_8 is labeled as *deleted*; (2) only P_8 or P_6 is labeled.

Meanwhile, there are four ways deciding the removal of the neighbors of P_1: (1) If P_2 and P_4 are labeled as *deleted*, P_2 and P_4 should be removed; (2) if P_6 and P_8 are *deleted* while P_5 and P_9 are not *deleted*, P_6 and P_8 should be removed; (3) if P_4 and P_6 are labeled as *deleted*, P_4 and P_6 should be removed; (4) if P_2 and P_8 are *deleted* while P_3 and P_7 are not *deleted*, P_2 and P_8 should be removed.

Refined results are shown in Fig. 3d. Boxes with the same color are corresponding to the same areas between rough and refined skeletons. The refined skeletons would have just one-pixel width and easy to be processed by our following procedures.

3.2 Topology identification

It is necessary to extract the key points to derive the topologies of the skeletons for further reconstruction. For bifurca-

tions, we adopt a pattern-matching method, in which the five basic patterns are shown in Fig. 3b and through changing these patterns by 90°, 180°, and 270°, all patterns could be found. On the other hand, for distal nodes, we examine its eight neighbors and select those that just have one neighbor. Extracted key points could be found in Fig. 2d. Bifurcation and distal nodes are labeled using filled circle marks.

Once the key points are extracted, skeleton segments are easy to be derived. Actually, skeleton segments start from bifurcation points and end at bifurcation or distal nodes. In our approach, we start from the bifurcation points and examine the eight neighbors of current point.

Since one skeleton line consists of two bifurcations or one bifurcation with one end point, skeleton segments extracted using this method are redundant because each bifurcation point is computed twice. Therefore, we transverse all the skeletons and remove duplicate segments. The skeleton segments are drawn in Fig. 2d. Different colors indicate different skeleton branches.

4 4D shape and motion reconstruction

Conventional image-based 3D reconstruction requires registration between different projection views. However, there are fewer features in the X-ray images than general camera images. Thus, it is hard to match the corresponding points between X-ray images reliably. The mistakes during registration may lead to much more severe errors during reconstruction. Meanwhile, it is also hard to add constraints such as the connectivity of the vessel neighbors, or prior knowledge for registration based methods, resulting in a significant waste of the various original information. Instead of relying on registration, we devise an algorithm to recover the initial shape of the 3D vessels as an energy minimization problem (Sect. 4.1). Meanwhile, the continuously moving frames provide strong clues for their subsequent frames. Based on the initial shapes, we generalize the above algorithm and design a robust motion tracking algorithm to reconstruct the dynamic vessels of the subsequent frames (Sect. 4.2).

4.1 Initial 3D reconstruction

Instead of using conventional image reconstruction methods, we bypass the registration issue and discretize the space between the optical center and the intensifier into voxels to formulate the 3D reconstruction problem as an energy minimization problem as described in Fig. 5. It is obvious that the unknown 3D skeleton should satisfy the following conditions: (1) the projection of every point of the 3D skeleton onto every 2D X-ray image is on the 2D skeleton; (2) the 3D skeleton is continuous with almost the same topology to the 2D skeleton except occlusion.

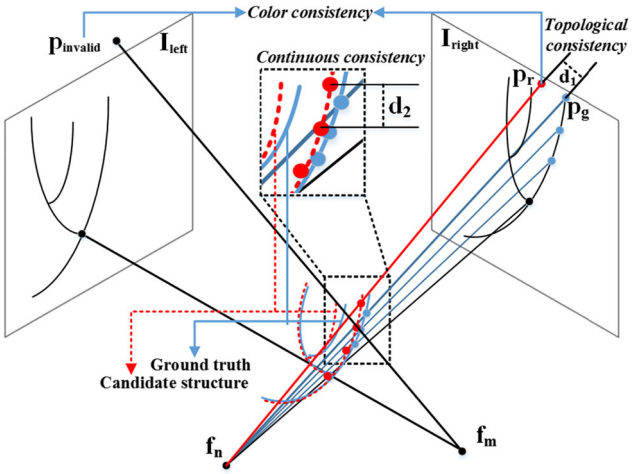

Fig. 4 Energy constraints determining the probability

Actually, the 3D skeletons could be regarded as a skeleton tree consisting of several skeleton segments or branches. Each segment could be seen as being made up of discretely sampled points. In order to solve the optimization problem, we quantize the 3D space into discrete voxels. Each 3D point p in the sampled space could be assigned with a probability of belonging to the 3D skeletons. The probability could be determined by the following terms which are described in Fig. 4:

- Number of views in which the projected point of p is valid, which is called color consistency.
- Distance between p and its neighbors in the same 3D skeleton to ensure continuity, which is called continuous consistency.
- Distance between the projected 2D point and its nearest valid 2D skeleton point on the same view, which is called topological consistency.

Finally, the sampled 3D space between the optical center and the intensifier is discretized into voxels and could be regarded as a Markov Random Field such that the reconstruction problem could be formulated as an energy minimization problem with color, continuous and topological constraints. We use three views of angiograms in a cardiac cycle and choose the projection view I_1 as a reference view with least foreshortening and overlapping among all the views. The 3D space is divided into 3D slices which we call layer $L = (l_1, l_2, \ldots, l_n)$ with a given depth interval. The 3D slicing and sampling is described in Fig. 5.

Each depth can be assigned with a label l_i. Meanwhile, each skeleton point on reference view I_1 corresponds to one projected line from the source to the intensifier through all the layers. Therefore, for a given pixel p on I_1, the pair (p, l_i) uniquely determines a point in 3D space. So, the goal of 3D

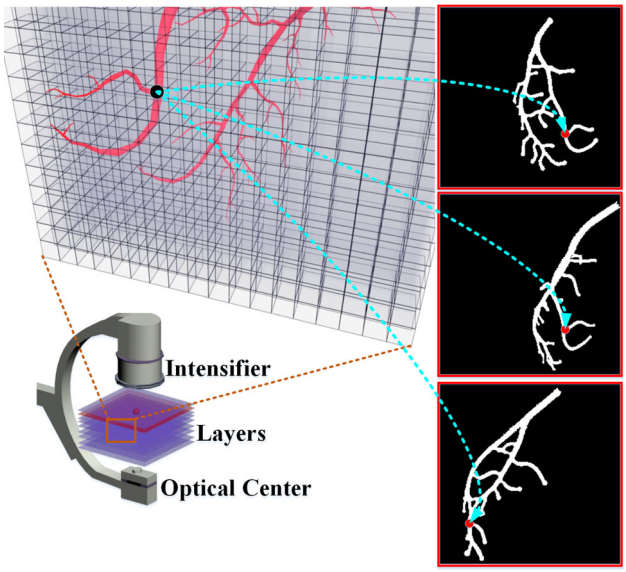

Fig. 5 3D space sampling

reconstruction is to optimally assign an label l_i to each p on the centerline of the reference view I_1. The energy function is defined as

$$E(f) = \sum_{p \in P} D_p(f_p) + \lambda \sum_{p,q \in N} V_{p,q}(f_p, f_q). \quad (1)$$

We define the $V_{p,q}(f_p, f_q)$ as the Euclidean distance to ensure the continuity between adjacent points p and q. And we define the $D_p(f_p)$ as the color consistency which is described as

$$D_p(f_p) = \frac{1}{(n-1)} \sum_{i=2}^{n} P_i(x, y), \quad (2)$$

where n is the number of back projected points, and $P_i(x, y)$ is the projection value of point p on the i-th view, which is defined as

$$P_i(x, y) = \begin{cases} W_h, & p(x, y) \in I_i \\ W_l, & \mathcal{N}(p(x, y)) \notin I_i \\ \frac{1}{N} \sum_{i=1}^{N} V_i(x, y), & \text{otherwise} \end{cases}, \quad (3)$$

where $p(x, y) \in I_i$ denotes that $p(x, y)$ is on the skeleton of I_i. W_h and W_l are two constants that control the highest and lowest value (in our experiments they are set to 0.01 and 1.0, respectively). For a gray-scale image, $\mathcal{N}(p(x, y))$ denotes point $p(x, y)$ and 8 neighbors of $p(x, y)$. In our methods, if $p(x, y)$ cannot be found in I_i, we compute its 8 neighbors and make the average value be the value of point $p(x, y)$. If none of its neighbors is valid, it is assigned to W_l.

We find the minimum of $E(f)$ using the Belief Propagation (BP) algorithm, which is comprised of two main steps, message propagation and energy minimization. In the message propagation step, the color of point $p(x, y) \in I_1$ is updated by

$$V_p = V_{p-1} + \alpha minD + (1 - \alpha) V_{p_{minD}}, \quad (4)$$

where α is a constant controlling the weight of the neighbors' color consistency and dist consistency. In our experiments, we set α to 0.85. $minD$ stands for the minimum distance from $p(x, y)$ to its neighbors, and $V_{p_{minD}}$ stands for the value of the minimum distance point. In our energy minimization, different from typical BP, the current energy of the i-th depth(l_i) is defined as

$$e_i(p_i) = min[\gamma D(p_i, q) + (1 - \gamma) V(q) + e_{i-1}(q)], \quad (5)$$

where q denotes the candidate 3D sample points corresponding to the projected point of $\mathcal{N}^o(p_i)$, and $\mathcal{N}^o(p_i)$ represents all neighbors of p_i except p_i itself.

At the end, we compute the minimum sum of all the grouped vessel skeletons' cost and obtain the optimal solution for the whole vessel skeleton tree. Now we have obtained the initial 3D shape of the vessels.

4.2 Dynamic reconstruction

Based on the initial reconstruction, we continue to generalize the above algorithm to track the vessel motions called Dynamic Reconstruction. Each image pair in the sequence could correspond to one special vessel skeleton in the motion sequence. Due to the characteristics of cardiac motion, these skeletons should be just changed slightly from its proceeding pose and changed slightly to its subsequent pose. Considering movement tracking of one frame to its next frame, reconstructed vessels of this frame can be regarded as prior knowledge to its subsequent pose. Deformed skeletons in the next frame should be close enough to the proceeding shape and the movement should be small. Since we treat the sample space as a discrete voxel space (a.k.a. Markov Random Field), this can be done by re-weighting the sampled valid points according to the distance to their corresponding prior points. Therefore, the energy term $E(f)$ from the standard energy is reformulated as

$$E^{'}(f) = E(f) + R_{p,k}(f_p, g_k), \quad (6)$$

where $R_{p,k}(f_p, g_k)$ is the new constraint to attract the shape not moving far away from its prior shape g_k. We use the minimum distance between p and its corresponding prior point k to evaluate p and re-weight its energy. $R_{p,k}(f_p, g_k)$ is a piecewise linear function based on $D_{p,g(k)}$ which is the minimum distance from p to the prior point. In our implementa-

tion, we set five pieces: [0,0.5], (0.5,1.0], (1.0,2.0], (2.0,5.0], (5.0, + ∞).

According to Eq. (6), points with distance close enough should be equipped with small energy and have more chances to be selected, while points with large distance should be equipped with high energy to penalize its score. Even worse, it might be considered to be deleted (ignored) from the candidate queue. In our implementation, we may have thousands of prior points and even millions of sampled candidate points. To compute the minimum distance efficiently, we design a three-dimensional kd-tree which provides the ability of searching nearest neighbors in $O(log(n))$ time. During each tracking frame, for every sampled point achieved from CUDA kernel, we compute its distance to the prior point and add up the weighted energy. Then, we use BP to compute the optimal solution. At the end, this optimized result is initialized as the prior shape for the next frame.

5 CUDA-based parallel algorithms

Our methods are evaluated carefully at the very start of attempting to design parallelized implementation for performance enhancement, which allows us to take the full advantage of CUDA in skeleton tracking and extraction and gain great efficiency in BP messaging. Image preprocessing with CUDA is described in Fig. 6. The angiograms are divided into image blocks and each pixel corresponds to one CUDA thread.

Parallelized vessel extraction. Since the computation on every pixel is independent, the vessel extraction algorithm is very suitable to be parallelized and every pixel is mapped to a CUDA thread for parallelization. For every angiogram among the imaging sequence and for every specified σ, our parallelized extraction method consists of the following steps. First, we build the Gaussian kernel mask depending on σ on CPU side and transfer them into the GPU. Second, we convolve the entire image using this Gaussian kernel and each pixel point on the image corresponds to one CUDA kernel. Third, we extract the eigenvalues and eigenvectors and compute the coefficients for each point's Hessian matrix. This is also done per kernel on GPU. Finally, we use a double-swap buffer on GPU to compute the possibility of being part of vessel structures for each pixel(refer to Eq. 15 of [9] for details). In all the procedures, except initialization, data are on GPU side and stored for further processing.

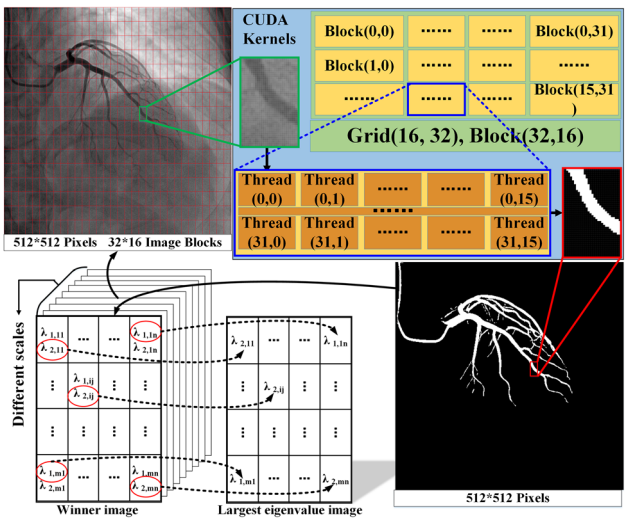

Fig. 6 GPU implementation for image preprocessing

Parallelized thinning. After vessel extraction, extracted vessels are stored on GPU to be further processed for skeleton tracking. During tracking, each valid vessel point is mapped to one CUDA kernel. In each kernel, we compute the point's eight neighbors and assign zero to those not fulfilling our thinning condition as described in Sect. 3.1. Finally, any points not belonging to the skeleton are removed.

In the key point extraction step, every valid point is mapped to one CUDA thread. For every point, we iterate four different degrees and five patterns (Fig. 3b) to identify whether it is a bifurcation. Meanwhile, points with just one neighbor are recognized as distal nodes.

Once we get the key points, we collect the skeletons in a parallelized way. Every bifurcation point is mapped to a CUDA thread and we perform nearest neighbor search in each CUDA kernel ending at either bifurcation or end point to extract skeleton segment.

Parallelized message propagation. Due to the serial characteristics of BP, we are unable to run it completely in parallel. Nonetheless, energy weighting based on distance computation among thousands of neighbor points during message propagation can be greatly accelerated by parallelization. In such situations, we implement a parallelized distance computation method with the help of CUDA which is described in Algorithm 1. The problem can be abstracted as follows: given two point vectors of dimension m and n, we intend to compute the minimum distances from every point of the first vector to the points of the second vector. We compute the $n \times m$ distance matrix using $n \times m$ CUDA threads and then search for the minimum values of every columns parallelly to derive a m vector. We normalize the vector and add it to the candidate energy values. Comparison for our parallelized message propagation and a classical BP is illustrated in Fig. 7. The horizontal axis indicates the number of processed points. The vertical axis shows the processing time. The blue line and red line, respectively, indicate processing method using CPU and GPU which have shown our method has gained great efficiency in message propagation.

Algorithm 1 Message Propagation

Input:
$pCandi$, sampled candidate points.
$pIMG$, 2D image. $szData$, sizes of skeletons.
$szLn$, line counts. $pNum$, 3D valid point counts
Output:
propagated candidate points.

function BPMESSAGE($pNum, pCandi, pIMG, szData, szLn$)
  $pCollect \leftarrow$COLLECTVALIDSIZE($pNum$)
  $nMAXVSZ \leftarrow max(pCollect)$
  $pCache \leftarrow allocCache(nMAXVSZ)$
  for $i = 0 \rightarrow ITERATIONS$ **do**
    BPMESSAGE_ONESTEP($pCandi, pCache$)
  end for
end function

function BPMESSAGE_ONESTEP($pCandi, pCache$)
  $pValid1 \leftarrow pCandi[i], pValid2 \leftarrow pCandi[j]$
  $fMinD \leftarrow$CUDAGETMIND($pValid1, pValid2, pCache$)
  for $k = 0 \rightarrow szValid1$ **do**
    $pValid1[k].fEnergy+ = fMinD$
  end for
end function

function CUDAGETMIND($pValid1, pValid2, pCache$)
  $threadId \leftarrow getGlobalIdx2D()$
  $nDataIdx \leftarrow getGlobalIdx1D()$
  $pCache[threadId] \leftarrow$DIST($pValid1[x], pValid2[y]$)
  $syncthreads()$
  $fMinD \leftarrow pCache[nDataIdx]$
  for $i = 0 \rightarrow nSZ0$ **do**
    if $pData[nDataIdx + i * nSZ1] < fMinD$ **then**
      $fMinD \leftarrow pData[nDataIdx + i * nSZ1]$
    end if
  end for
  return $fMinD$
end function

function COLLECTVALIDSIZE($pValidPtsNum$)
  $threadId \leftarrow getGlobalIdx2D()$
  if $threadId > IMAGE\_DIM$ **then return** ;
  end if
  if $pValidPtsNum[threadId] > 0$ **then**
    $n \leftarrow atomicAdd(gValidCounter, 1)$
    $pDEVValidSZ[n] \leftarrow pValidPtsNum[threadId]$
  end if
end function

6 Experiments and validation

6.1 Data acquisition

Among all the procedures, we use two types of imaging data: synthetic data from our simulation platform and real clinical data captured by one Philip single-plane X-ray machine from Beijing Union Hospital. The alias of view angles in X-ray radiography are illustrated in Fig. 8.

For synthetic data, we use three different views, respectively, at RAO 50, LAO 50, LAO 0, while retaining the same CRA angle. In total, one sequence consisting of 130 synthetic

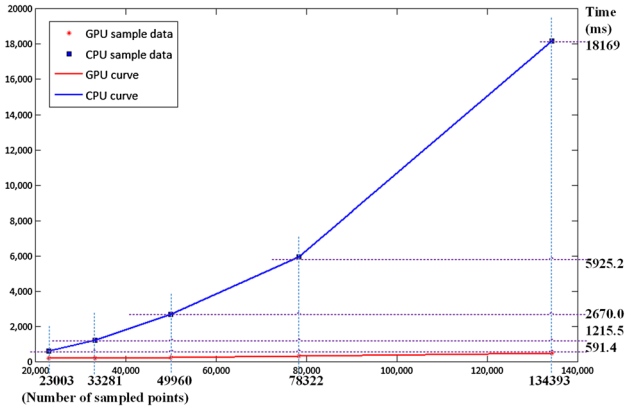

Fig. 7 Comparison of BP on CPU and GPU. The time cost of CPU implementation increases fast while the sampled points increase

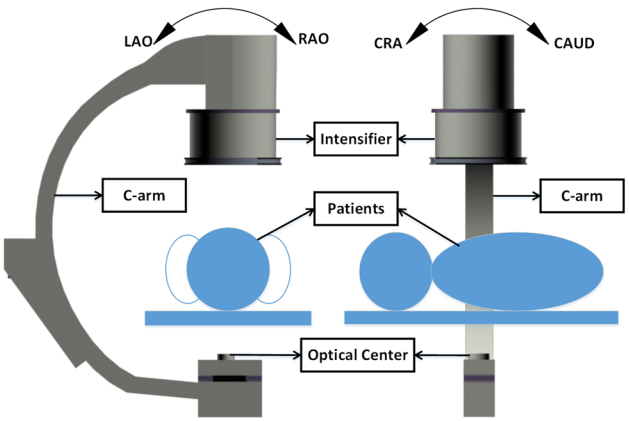

Fig. 8 View angles in medical imaging

image pairs is used to validate the reconstruction results and their efficiency.

For real data, seven sequences of X-ray images are used to validate our method and the corresponding view angles are listed in Table 1. Validation image pairs count and the first selected image pair indices are also illustrated. All the sequences of the views consist of at least 50 images with the pixel resolution of 512 × 512. As illustrated in Table 1, from each data, various numbers of image pairs, which is 131 in total, are selected to validate our reconstruction method.

For both synthetic and real data, ECG-Gating is used to select images at mostly the same cardiac cycle from each view.

6.2 Results

The reconstruction method is tested on both synthetic data and real clinical data which are definitely acquired at 5FPS and 15FPS for 512 × 512 images. Compared with the real data, the reconstruction of synthetic data is easy to be

Table 1 Data table for each clinical data set

Data set	Sequence view angles ($\theta°$)						Total image count			Selected image			Valid count
	LAO	CRA	RAO	CRA	LAO	CRA							
1	**32**	**27**	*25*	*29*	***2***	***29***	**61**	*57*	***57***	**27**	*34*	***38***	20
2	**29**	**23**	*33*	*23*	***2***	***23***	**53**	*47*	***49***	**24**	*29*	***31***	17
3	**44**	**24**	*32*	*24*	***−4***	***24***	**58**	*52*	***57***	**28**	*33*	***25***	19
4	**31**	**27**	*32*	*27*	***1***	***27***	**75**	*66*	***65***	**53**	*46*	***55***	12
5	**31**	**27**	*32*	*24*	***−2***	***23***	**65**	*54*	***83***	**29**	*37*	***35***	20
6	**40**	**28**	*29*	*31*	***4***	***27***	**57**	*54*	***66***	**36**	*45*	***34***	13
7	**31**	**22**	*30*	*25*	***3***	***25***	**66**	*66*	***68***	**30**	*37*	***32***	30

Bold: Left view data sets
Italic: Right view data sets
Bold Italic: Middle view data sets

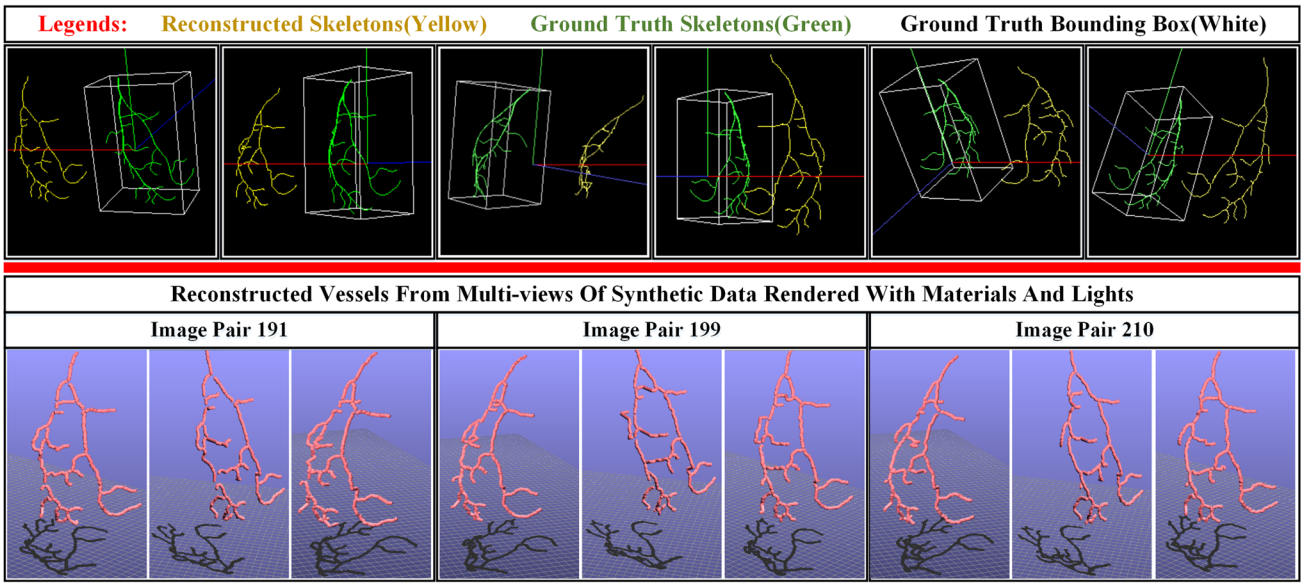

Fig. 9 Results of the synthetic data

assessed because of the availability of the vessel ground truth.

The final reconstruction results of synthetic data are shown in Fig. 9. In the top row of Fig. 9, the yellow lines indicate the reconstructed skeletons using our method. The green lines indicate the ground truth of the synthetic data. The white box is the bounding box of the ground truth. The second row represents three pairs of reconstructed vessels with materials and lights. Our synthetic data are from image pair 170 to image pair 299, 130 pairs in total. The pairs 191, 199, and 210 being drawn, are three out of the 130 reconstructed vessels and they have exhibited almost the same topology and continuity compared with the ground truth skeleton in the top row.

Meanwhile, eight frames from synthetic data are shown on the top row of Fig. 13 and the reconstructed vessels are shown in the bottom row. It may be noted that we can reconstruct the vessels' motion as well.

Real clinical data contain more noise or even incomplete information leading to more complex reconstruction. We evaluate our method based on seven data sets and totaly 131 image pairs. Nine pairs of the reconstructed dynamic vessels are shown in Fig. 10. We use color codes to specify the corresponding data set and selected image numbers. All results from the seven data sets are shown including three from data set 1 and one from data 2–7, respectively.

6.3 Validation

In order to evaluate the precision of our algorithm, we project the reconstructed skeletons back onto the image plane and

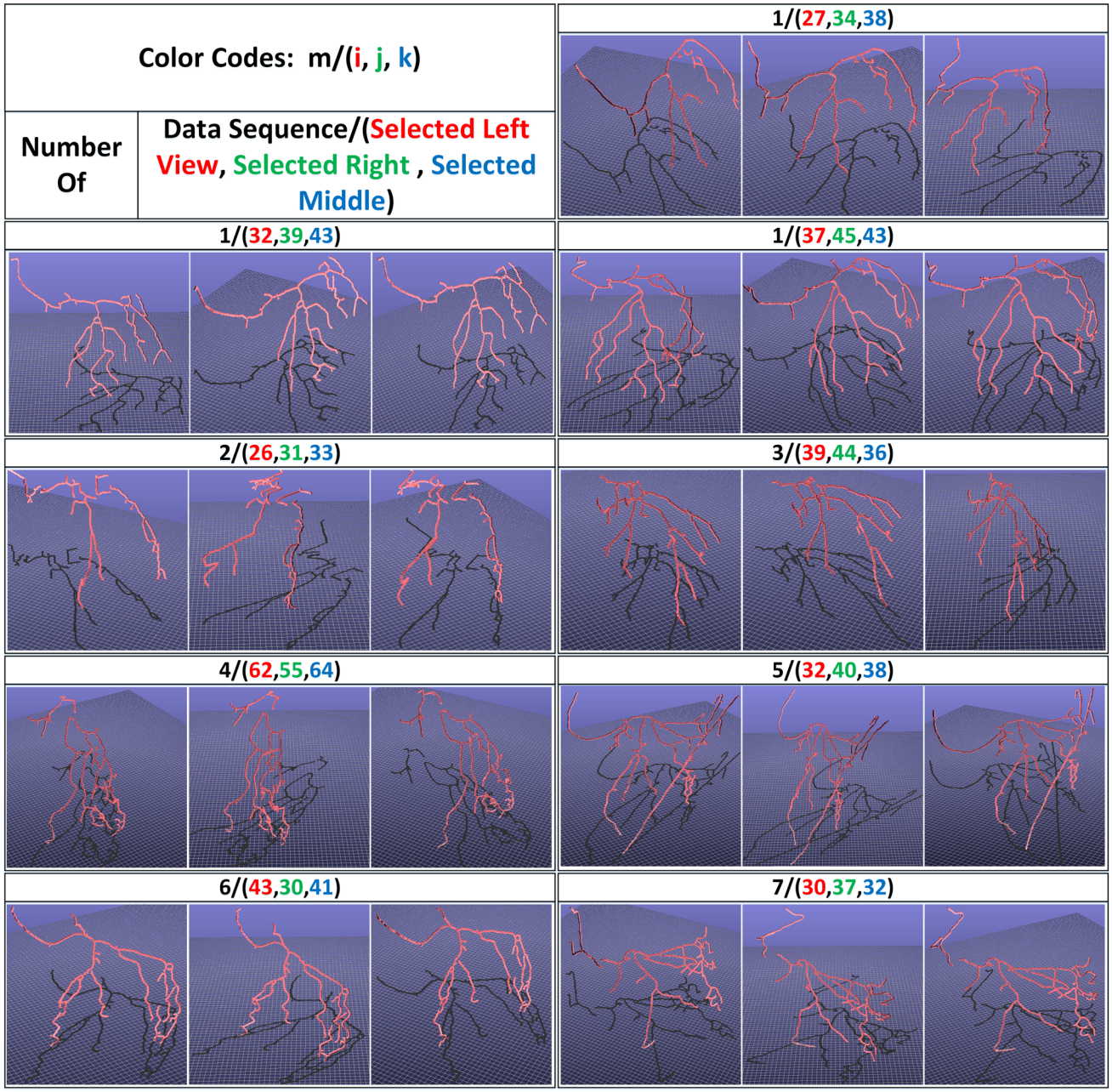

Fig. 10 Results from real data. Seven data sets are considered. Nine reconstructed pairs are presented including three for data set 1 and one for data set 2–7, respectively. Color codes are used to specify the number of the data set and selected views

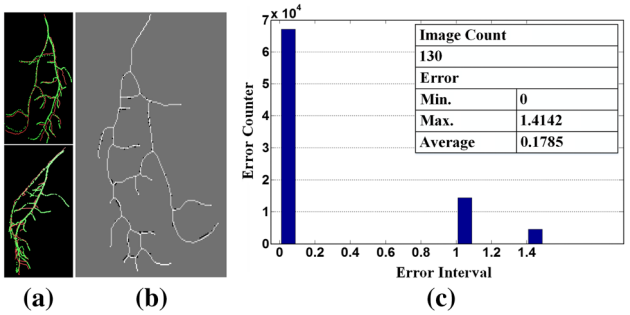

Fig. 11 One of re-projected error of the synthetic data and ground truth

compute the minimum distance between the ground truth and the projected vessels.

For synthetic data, Fig. 11a shows the 3D ground truth and reconstructed skeletons. Figure 11b shows one of the projected ground truth and the reconstructed skeletons. Figure 11c shows the error statistics. From Fig. 11c: it is obvious that most errors lie in the interval [0, 0.1] and we gain the maximum error 1.4142 and average error 0.1785 which show our algorithms' great accuracy.

For clinical data, Fig. 12 shows the error statistics for each data set. The last two of Fig. 12 specify the total sta-

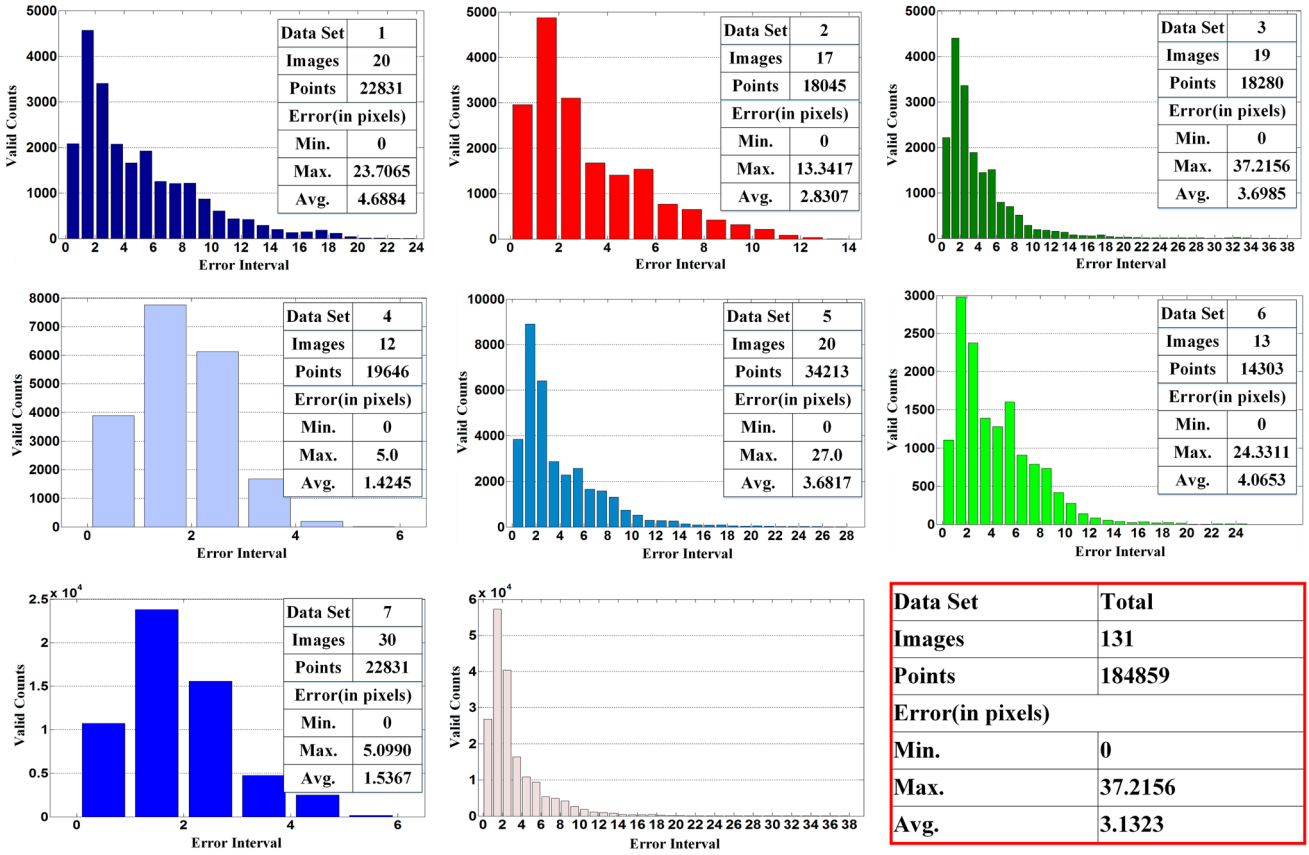

Fig. 12 Grouped re-projected error of the clinical data. Errors for each data set 1–7 are represented. The last one shows the total error analysis

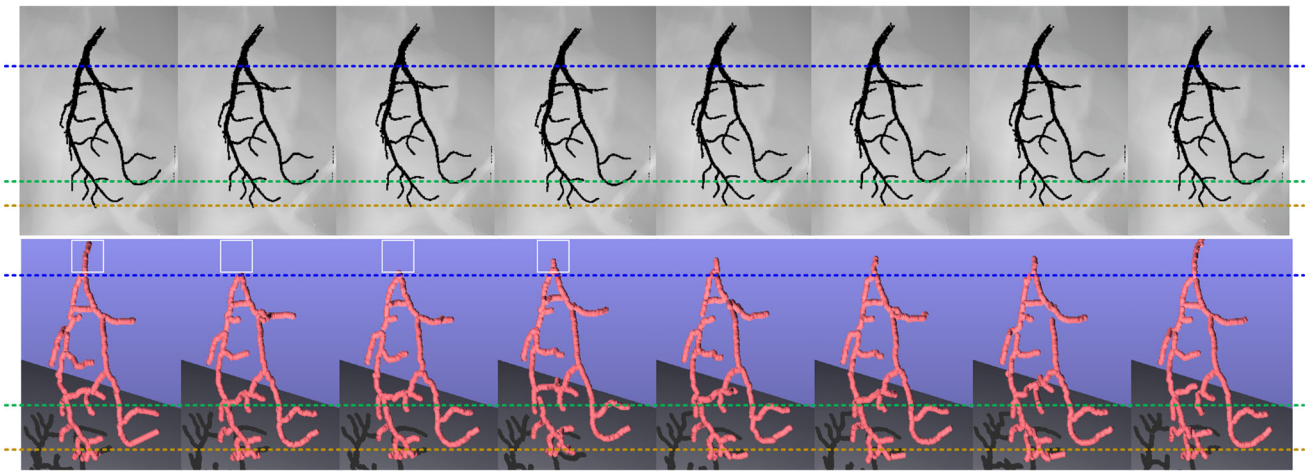

Fig. 13 Vessel motion tracking between sequential frames

tistics of the whole seven data sets with an average error of 3.1323 which indicates our method's promising accuracy, too.

For both Figs. 11c and 12, the X axis represents the error *interval*. For example, the bar in [0, 1] represents the number of valid points with error less than 1 pixel. Errors of most points are mostly distributed near the lower endpoints of the histogram which also demonstrates high accuracy of our method.

Because of heavily blurred and incomplete image data, some errors may occur during reconstruction in some frames as shown in the second frame of Fig. 13. The vessels marked in the white rectangle are missing in the second frame and they are recovered in the following frames, illustrating the

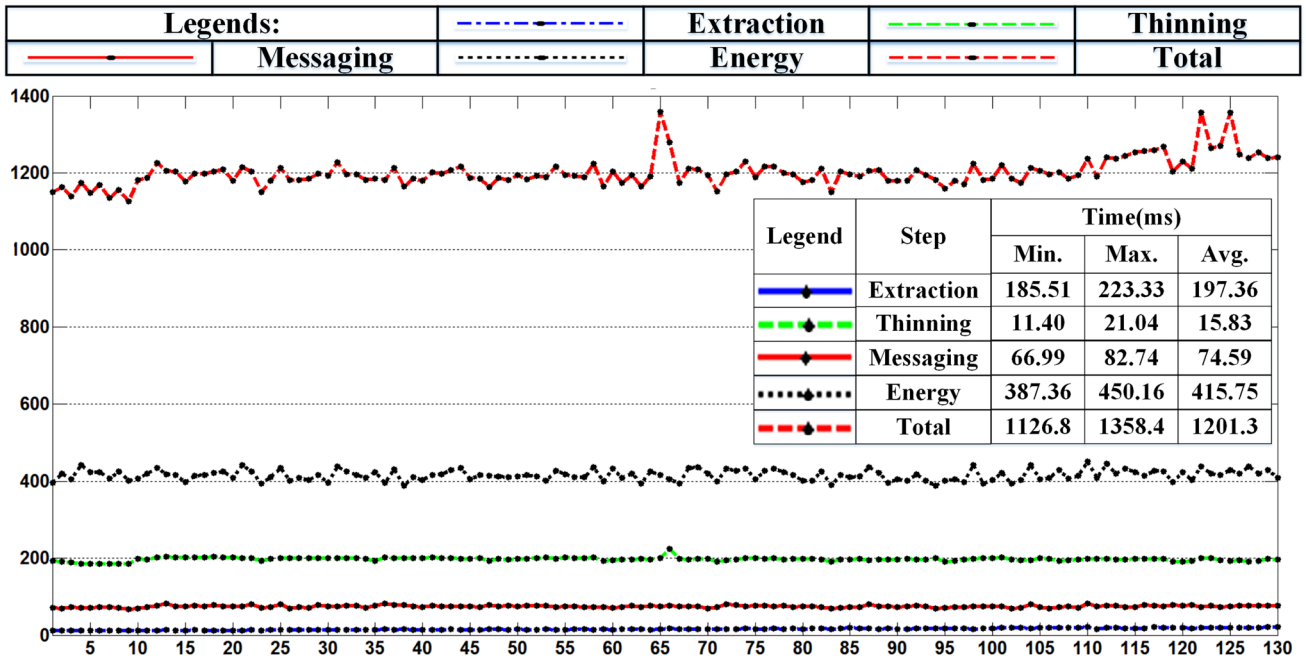

Fig. 14 The overall time analysis together with the detailed statistics of each step based on 130 frames of synthetic data

Data Set	Validation Count
1	20
2	17
3	19
4	12
5	20
6	13
7	30

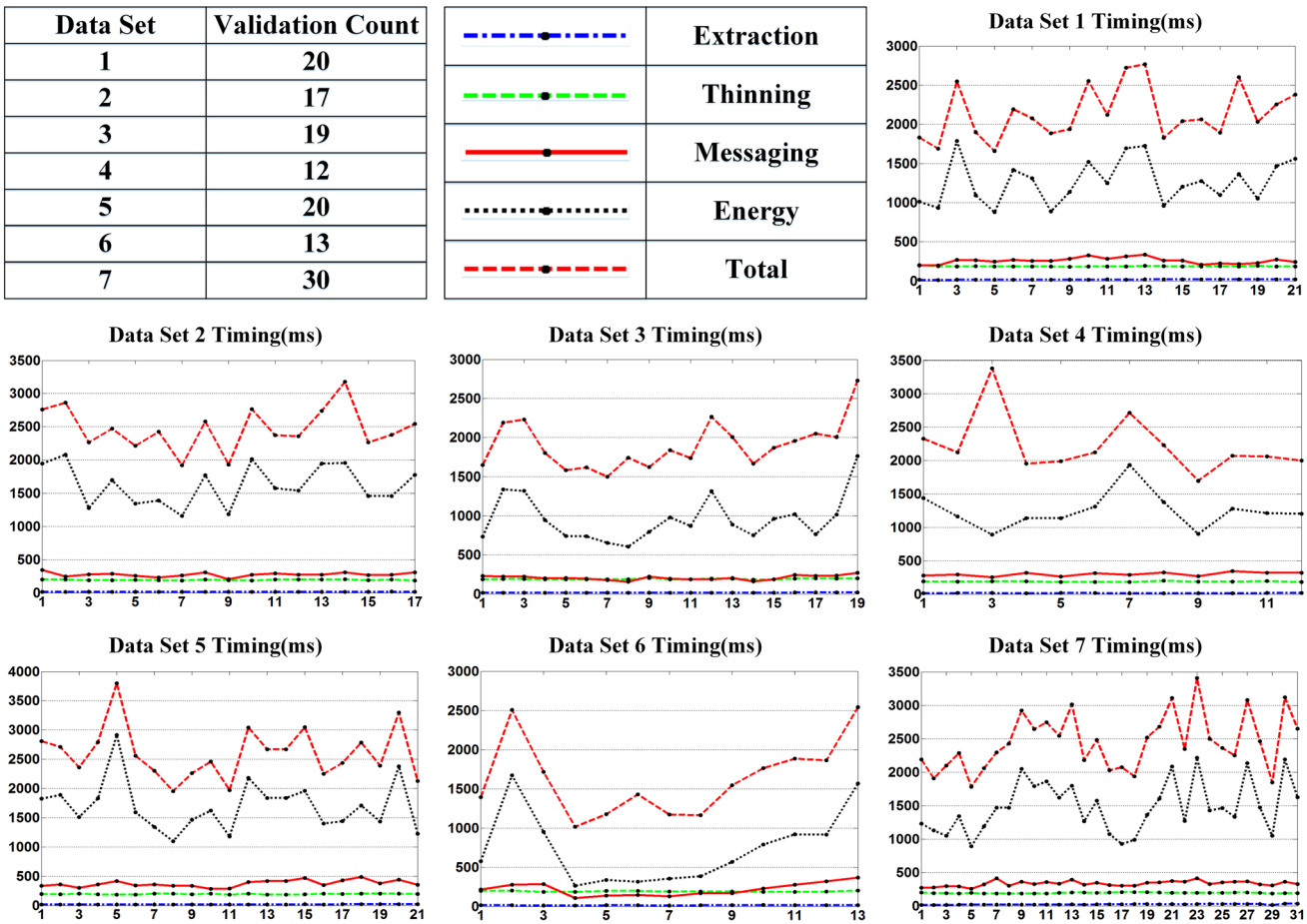

Fig. 15 The overall time analysis together with the detailed statistics of each step with data set 1–7, respectively. The last one shows the total time analysis

Table 2 The overall numerical time statistics for data set 1–7, respectively. The last one shows the total time statistics

	Time Statistics(ms)											
	Data Set 1			Data Set 2			Data Set 3			Data Set 4		
Step	Min.	Max.	Avg.	Min.	Max.	Avg.	Min.	Max.	Avg.	Min.	Max.	Avg.
Extraction	182.45	202.64	187.09	182.53	205.59	192.53	184.92	204	191.55	179.57	202.11	187.72
Thinning	12.586	21.365	17.016	12.127	17.28	13.637	13.448	20.603	16.222	12.925	17.471	15.493
Message	198.92	337.3	258.55	206.13	341.02	274.34	157.13	271.64	208	251.3	347.01	299.25
Energy	878.95	1786	1267	1157	2078	1621	604.46	1761	959.09	895.01	1933	1249
Total	1657	2765	2140	1920	3178	2471	1498	2730	1897	1694	3379	2220
	Data Set 5			Data Set 6			Data Set 7			Total		
Step	Min.	Max.	Avg.	Min.	Max.	Avg.	Min.	Max.	Avg.	Min.	Max.	Avg.
Extraction	184.19	202.94	194.29	183.01	201.36	191.83	184.41	204.55	194.1	**179.57**	**205.59**	**191.3**
Thinning	13.723	22.768	16.676	12.167	17.451	14.291	13.382	31.074	21.785	**12.127**	**31.074**	**16.446**
Message	280.94	488.07	373.34	105.83	368.46	216.83	254.27	413.25	332.54	**105.83**	**488.07**	**280.4**
Energy	1096	2914	1698	261.14	1672	739.17	890.48	2213	1481	**261.14**	**2914**	**1288**
Total	1951	3801	2604	1014	2541	1627	1782	3406	2449	**1014**	**3801**	**2201**

robustness of our method that could also combat the incomplete data.

6.4 Efficiency analysis

Since we have designed and selected the algorithm at the very beginning carefully, our methods have gained great efficiency. Time analysis is also done on both synthetic and clinical data.

Time analysis for synthetic data is quantized and shown in Fig. 14. Different legends are used to specify the time of steps in our method. We show the time consumption for each step of the 130 validation data. The preprocessing step *Extraction* and *Thinning* are near 200 ms in total, and the total time is around 1200ms. Since the vessel structures from each image pair is simple and much alike, all the statistics are stable, which is explained by the smoothness of the fitting curves.

On the other side, as with clinical data, detailed statistics of each step for the data set 1–7 are shown in Fig. 15. Validation count and corresponding legends are also listed. The corresponding numerical statistics are shown in Table 2, illustrating the minimum, maximum, and average time consumption for each step of each data set. We can observe that, as real data are much more complex than synthetic data, the processing time tends to be longer. However, since the preprocessing step is greatly parallelized with CUDA, the preprocessing time only increases slightly. Most of the time costs are consumed in the energy optimization step because of the characteristics of BP.

All these experiments are carried on a workstation with one NVIDIA GTX-780 GPU, one Intel(R) Core(TM) i7-3770 CPU(3.4GHz) and 8GB RAM. Visual Studio and CUDA 5 are installed on Windows 7 of this workstation. CUDA compute capability 3.5 is enabled to use the dynamic parallelism feature.

6.5 Discussion

Compared with typical registration methods, our method avoids explicit registration, converts it into an energy minimization problem, and designs a flexible framework with various constraints. Based on this framework, combined with the global nature of BP, our reconstruction is more robust compared to typical registration methods, especially for incomplete data. Besides, with the help of CUDA, our reconstruction algorithm gains high efficiency. The average reconstruction time is 3 s for clinical data and 1.2 s for synthetic data, which is much faster than classical methods.

7 Conclusion

We have developed a new 4D dynamic vessel reconstruction system from X-ray angiograms. The uniqueness of our system is its simultaneous handling on structure, shape, and motion during vessel reconstruction. The technical core of our system are the parallel algorithms towards interactive performance. Specifically, at the vessel skeleton extraction stage, we developed an efficient parallel method to extract vessels as well as their skeleton and topology from X-ray views. At the reconstruction stage, we formulate the dynamic reconstruction problem as an energy optimization problem solved by BP without explicit registration. The experimental results from both synthetic and clinical data have shown that our method is robust for noise and even incomplete data

because of the algorithms' global optimization nature. Our immediate goal for ongoing work is to continue to improve our system and its functionalities towards clinic trial in the near future.

Acknowledgments This work was supported in part by National Natural Science Foundation of China (Grant No. 61190120, 61190121, 61190125, 61300068, 61300067), National Science Foundation of USA (Grant No. IIS-0949467, IIS-1047715, and IIS-1049448), the National High Technology Research and Development Program (863 Program) of China (Grant No. 012AA011503), Postdoctoral Science Foundation of China (Grant No. 2013M530512).

References

1. Sarry, L., Boire, J.-Y.: Three-dimensional tracking of coronary arteries from biplane angiographic sequences using parametrically deformable models. IEEE Trans. Med. Imaging **20**(12), 1341–1351 (2001)
2. Cañero, C., Vilariño, F., Mauri, J., Radeva, P.: Predictive (un) distortion model and 3-d reconstruction by biplane snakes. IEEE Trans. Med. Imaging **21**(9), 1188–1201 (2002)
3. Dumay, A.C., Gerbrands, J.J., Reiber, J.H.: Automated extraction, labelling and analysis of the coronary vasculature from arteriograms. Int. J. Card. Imaging **10**(3), 205–215 (1994)
4. Aylward, S.R., Bullitt, E.: Initialization, noise, singularities, and scale in height ridge traversal for tubular object centerline extraction. IEEE Trans. Med. Imaging **21**(2), 61–75 (2002)
5. Sen, A., Lan, L., Doi, K., Hoffmann, K.R.: Quantitative evaluation of vessel tracking techniques on coronary angiograms. Med. Phys. **26**(5), 698–706 (1999)
6. Kirbas, C., Quek, F.: A review of vessel extraction techniques and algorithms. ACM Comput. Surv. (CSUR) **36**(2), 81–121 (2004)
7. Hoover, A., Kouznetsova, V., Goldbaum, M.: Locating blood vessels in retinal images by piecewise threshold probing of a matched filter response. IEEE Trans. Med. Imaging **19**(3), 203–210 (2000)
8. Li, Q., You, J., Zhang, D.: Vessel segmentation and width estimation in retinal images using multiscale production of matched filter responses. Expert Syst. Appl. **39**(9), 7600–7610 (2012)
9. Frangi, A.F., Niessen, W.J., Vincken, K.L., Viergever, M.A.: Multiscale vessel enhancement filtering. In: MICCAI'98, Springer. pp. 130–137 (1998)
10. Condurache, A.-P., Aach, T.: Vessel segmentation in angiograms using hysteresis thresholding. In: IAPR Conference on Machine Vision Applications, pp. 269–272 (2005)
11. Zhang, B., Zhang, L., Zhang, L., Karray, F.: Retinal vessel extraction by matched filter with first-order derivative of gaussian. Comput. Biol. Med. **40**(4), 438–445 (2010)
12. Van Uitert, R., Bitter, I.: Subvoxel precise skeletons of volumetric data based on fast marching methods. Med. Phys. **34**(2), 627–638 (2007)
13. Hassouna, M., Farag, A.: Multistencils fast marching methods: a highly accurate solution to the eikonal equation on cartesian domains. IEEE Trans. Pattern Anal. Mach. Intell. **29**(9), 1563–1574 (2007). doi:10.1109/TPAMI.2007.1154
14. Zhang, T.Y., Suen, C.Y.: A fast parallel algorithm for thinning digital patterns. Commun. ACM **27**(3), 236–239 (1984)
15. Wellnhofer, E., Wahle, A., Mugaragu, I., Gross, J., Oswald, H., Fleck, E.: Validation of an accurate method for three-dimensional reconstruction and quantitative assessment of volumes, lengths and diameters of coronary vascular branches and segments from biplane angiographic projections. Int. J. Card. Imaging **15**(5), 339–353 (1999)
16. Messenger, J.C., Chen, S.J., Carroll, J.D., Burchenal, J., Kioussopoulos, K., Groves, B.M.: 3d coronary reconstruction from routine single-plane coronary angiograms: clinical validation and quantitative analysis of the right coronary artery in 100 patients. Int. J. Card. Imaging **16**(6), 413–427 (2000)
17. Gollapudi, R.R., Valencia, R., Lee, S.S., Wong, G.B., Teirstein, P.S., Price, M.J.: Utility of three-dimensional reconstruction of coronary angiography to guide percutaneous coronary intervention. Catheter. Cardiovasc. Interv. **69**(4), 479–482 (2007)
18. Movassaghi, B., Rasche, V., Grass, M., Viergever, M.A., Niessen, W.J.: A quantitative analysis of 3-d coronary modeling from two or more projection images. IEEE Trans. Med. Imaging **23**(12), 1517–1531 (2004)
19. Sprague, K., Drangova, M., Lehmann, G., Slomka, P., Levin, D., Chow, B., et al.: Coronary x-ray angiographic reconstruction and image orientation. Med. Phys. **33**, 707–718 (2006)
20. Hansis, E., Schäfer, D., Dössel, O., Grass, M.: Projection-based motion compensation for gated coronary artery reconstruction from rotational x-ray angiograms. Phys. Med. Biol. **53**(14), 3807–3820 (2008)
21. Nguyen, T.V., Sklansky, J.: Reconstructing the 3-d medial axes of coronary arteries in single-view cineangiograms. IEEE Trans. Med. Imaging **13**(1), 61–73 (1994)
22. Fessler, J.A., Macovski, A.: Object-based 3-d reconstruction of arterial trees from magnetic resonance angiograms. IEEE Trans. Med. Imaging **10**, 25–39 (1991)
23. Liu, I., Sun, Y.: Fully automated reconstruction of three-dimensional vascular tree structures from two orthogonal views using computational algorithms and productionrules. Opt. Eng. **31**(10), 2197–2207 (1992)
24. Weng, J., Ahuja, N., Huang, T.S.: Optimal motion and structure estimation. IEEE Trans. Pattern Anal. Mach. Intell. **15**(9), 864–884 (1993)
25. Chen, S.-Y.J., Hoffmann, K.R., Carroll, J.D.: Three-dimensional reconstruction of coronary arterial tree based on biplane angiograms. Proc. SPIE Med. Imag. Image Process. **2710**, 103–114 (1996)
26. Chen, S.Y.J., Metz, C.E.: Improved determination of biplane imaging geometry from two projection images and its application to 3-d reconstruction of coronary arterial trees. Med. Phys. **24**, 633–654 (1997)
27. Ruan, S., Bruno, A., Coatrieux, J.-L.: Three-dimensional motion and reconstruction of coronary arteries from biplane cineangiography. Image Vis. Comput. **12**(10), 683–689 (1994)
28. Puentes, J., Roux, C., Garreau, M., Coatrieux, J.-L.: Dynamic feature extraction of coronary artery motion using dsa image sequences. IEEE Trans. Med. Imaging **17**(6), 857–871 (1998)
29. Ingrassia, C., Windyga, P., Shah, M.: Segmentation and tracking of coronary arteries. In: BMES/EMBS Conference, vol. 1, IEEE, pp. 203–203 (1999)
30. Chen, S.-Y., Carroll, J.D.: Kinematic and deformation analysis of 4-d coronary arterial trees reconstructed from cine angiograms. IEEE Trans. Med. Imaging **22**(6), 710–721 (2003)
31. Naegel, B., Passat, N., Ronse, C.: Grey-level hit-or-miss transforms-Part I: unified theory. Pattern Recognit. **40**(2), 635–647 (2007)
32. Shechter, G., Devernay, F., Coste-Manière, E., Quyyumi, A., McVeigh, E.R.: Three-dimensional motion tracking of coronary arteries in biplane cineangiograms. IEEE Trans. Med. Imaging **22**(4), 493–503 (2003)
33. Shechter, G., Resar, J.R., McVeigh, E.R.: Displacement and velocity of the coronary arteries: cardiac and respiratory motion. IEEE Trans. Med. Imaging **25**(3), 369–375 (2006)
34. Blondel, C., Malandain, G., Vaillant, R., Ayache, N.: Reconstruction of coronary arteries from a single rotational x-ray projection sequence. IEEE Trans. Med. Imaging **25**(5), 653–663 (2006)

35. Bouattour, S., Arndt, R., Paulus, D.: 4D reconstruction of coronary arteries from monoplane angiograms. In: Computer Analysis of Images and Patterns, Springer. pp. 724–731 (2005)
36. Schoonenberg, G., Florent, R., Lelong, P., Wink, O., Ruijters, D., Carroll, J., ter Haar, B.: Projection-based motion compensation and reconstruction of coronary segments and cardiac implantable devices using rotational x-ray angiography. Med. Image Anal. **13**(5), 785–792 (2009)
37. Geman, S., Geman, D.: Stochastic relaxation, gibbs distributions, and the bayesian restoration of images. IEEE Trans. Pattern Anal. Mach. Intell. **6**, 721–741 (1984)
38. Lafferty, J.D., McCallum, A., Pereira, F.C.N.: Conditional random fields: probabilistic models for segmenting and labeling sequence data. In: Proceedings of the Eighteenth International Conference on Machine Learning, ICML '01, Morgan Kaufmann Publishers Inc., San Francisco, CA, USA, pp. 282–289 (2001)
39. Pearl, J.: Reverend bayes on inference engines: a distributed hierarchical approach. AAAI. pp. 133–136 (1982)
40. Meltzer, T., Yanover, C., Weiss, Y.: Globally optimal solutions for energy minimization in stereo vision using reweighted belief propagation. In: Proceedings of the Tenth IEEE International Conference on Computer Vision, ICCV '05, IEEE Computer Society, pp. 428–435 (2005)
41. Murphy, K.P., Weiss, Y., Jordan, M.I.: Loopy belief propagation for approximate inference: An empirical study. In: Proceedings of the Fifteenth conference on Uncertainty in artificial intelligence, Morgan Kaufmann Publishers Inc. pp. 467–475 (1999)
42. Szeliski, R., Zabih, R., Scharstein, D., Veksler, O., Kolmogorov, V., Agarwala, A., Tappen, M., Rother, C.: A comparative study of energy minimization methods for markov random fields with smoothness-based priors. IEEE Trans. Pattern Anal. Mach. Intell. **30**(6), 1068–1080 (2008)
43. Tappen, M.F., Freeman, W.T.: Comparison of graph cuts with belief propagation for stereo, using identical mrf parameters. In: Ninth IEEE International Conference on Computer Vision, IEEE, pp. 900–906 (2003)
44. Potetz, B., Lee, T.S.: Efficient belief propagation for higher-order cliques using linear constraint nodes. Comput. Vis. Image Underst. **112**(1), 39–54 (2008)
45. Brunton, A., Shu, C., Roth, G.: Belief propagation on the gpu for stereo vision. In: The 3rd Canadian Conference on Computer and Robot Vision, pp. 76–76 (2006)
46. Coughlan, J., Shen, H.: Dynamic quantization for belief propagation in sparse spaces. Comput. Vis. Image Underst. **106**(1), 47–58 (2007)
47. Felzenszwalb, P.F., Huttenlocher, D.P.: Efficient belief propagation for early vision. Int. J. Comput. Vis. **70**(1), 41–54 (2006)
48. Boykov, Y.Y., Jolly, M.-P.: Interactive graph cuts for optimal boundary & region segmentation of objects in nd images. In: Eighth IEEE International Conference on Computer Vision, vol. 1, pp. 105–112 (2001)
49. Boykov, Y., Veksler, O., Zabih, R.: Fast approximate energy minimization via graph cuts. IEEE Trans. Pattern Anal. Mach. Intell. **23**(11), 1222–1239 (2001)
50. Kolmogorov, V., Zabin, R.: What energy functions can be minimized via graph cuts? IEEE Trans. Pattern Anal. Mach. Intell. **26**(2), 147–159 (2004)
51. Vezhnevets, V., Konouchine, V.: Growcut: Interactive multi-label nd image segmentation by cellular automata. In: Proc. of Graphicon, pp. 150–156 (2005)
52. Rother, C., Kolmogorov, V., Blake, A.: Grabcut: Interactive foreground extraction using iterated graph cuts. ACM Trans. Gr. (TOG) ACM. **23**, 309–314 (2004)

Xinglong Liu received the master degree in computer science from Yantai University in 2010. He is currently working toward the Ph.D degree in the State Key Laboratory of Virtual Reality Technology and Systems at Beihang University. His research interests include 3D modeling, reconstruction and medical image processing.

Fei Hou received his Ph.D. degree of computer science from Beihang University and currently he is a post doctoral researcher at Beihang University. His research interests are medical image processing, image based modeling and data vectorization etc.

Aimin Hao Ph.D., born in 1968, is a professor of Computer School, Beihang University and the vice director of State Key Laboratory of Virtual Reality Technology and Systems. His research interests are virtual reality, database application and information system development.

Hong Qin received the BS and MS degrees in computer science from Peking University, China. He received the Ph.D degree in computer science from the University of Toronto (UofT) in 1995. He is a full professor of computer science in the Department of Computer Science at State University of New York at Stony Brook (Stony Brook University). During his years at the University of Toronto, he received UofT Open Doctoral Fellowship. He was also a recipient of NSF CAREER Award

from the US National Science Foundation (NSF), Honda Initiation Award, and Alfred P. Sloan Research Fellow by the Sloan Foundation. Currently, he serves as an associate editor for The Visual Computer, Graphical Models, and Journal of Computer Science and Technology. His research interests include geometric and solid modeling, graphics, physics-based modeling and simulation, computer aided geometric design, human-computer interaction, visualization, and scientific computing. Detailed information about him can be found from his website: http://www.cs.sunysb.edu/~qin. He is a senior member of the IEEE and the IEEE Computer Society.